Space Weather®

Unfolding the Neutron Flux Spectrum on the Surface of Mars Using the MSL-RAD and Odyssey-HEND Data

L. M. Martinez Sierra[1], **I. Jun[1]**, **B. Ehresmann[2]**, **C. Zeitlin[3]**, **J. Guo[4,5,6]**, **M. Litvak[7]**, **K. Harshman[8]**, **D. Hassler[2]**, **I. G. Mitrofanov[7]**, **D. Matthiä[9]**, and **S. Loffler[6]**

[1]Jet Propulsion Laboratory, California Institute of Technology, Pasadena, CA, USA, [2]Space Science and Engineering Division, Southwest Research Institute, Boulder, CO, USA, [3]Leidos Corporation, Houston, TX, USA, [4]Deep Space Exploration Laboratory/School of Earth and Space Sciences, University of Science and Technology of China, Hefei, People's Republic of China, [5]CAS Center for Excellence in Comparative Planetology, University of Science and Technology of China, Hefei, People's Republic of China, [6]Institute of Experimental and Applied Physics, Christian-Albrechts-University, Kiel, Germany, [7]Space Research Institute, RAS, Moscow, Russia, [8]Lunar and Planetary Laboratory, Department of Planetary Sciences, University of Arizona, Tucson, AZ, USA, [9]German Aerospace Center, Institute of Aerospace Medicine, Cologne, Germany

Abstract Understanding the long-term radiation environment at the surface of Mars allows us to estimate the exposure for future robotic and crewed missions. Typically, the radiation environment includes charged particles (i.e., protons and heavier ions) and neutral particles (i.e., gamma rays and secondary neutrons). Previous studies used in-situ measurements, models, or both to determine the characteristics of the radiation at Mars. For example, the Mars Science Laboratory instrument, the Radiation Assessment Detector (RAD), has provided invaluable in-situ data since landing in 2012. However, the RAD instrument is only sensitive to neutrons with energies > ~6 MeV and therefore misses what is expected to be a substantial flux of lower-energy neutrons. To address this gap, we have developed an approach to derive the surface neutron spectrum using the MSL RAD data augmented by orbital data from the High Energy Neutron Detector (HEND) onboard Mars Odyssey (neutron energy < ~10 MeV). Using a power law fit, we determine neutron flux spectra that reproduce the measurements recorded by both RAD and HEND. Our approach involves a series of Monte Carlo simulations to develop a set of atmospheric transmission functions that enables us to convert the on-orbit HEND data to their corresponding surface neutron flux spectra. The combined RAD—HEND data present a unique opportunity to obtain a complete picture of the surface neutron environment.

Plain Language Summary Unlike Earth, Mars does not possess an intrinsic magnetic field or a thick atmosphere to shield it from hostile space radiation. In this paper, we provide a methodology to predict how many neutrons will be present on the surface of Mars. We found that the number of neutrons on the surface varies with the Martian seasons and the Solar activity. Knowing the neutron environment allows us to determine the risks to future Mars crewed and robotic missions from neutron exposure.

1. Introduction

In the past five decades, Mars exploration missions have rapidly evolved. The first missions consisted of fly-by probes, followed by orbiters and landers. Now there are robotic roving laboratories (e.g., Curiosity, Grotzinger et al., 2012 and Perseverance, Farley et al., 2020; Grotzinger et al., 2012), and even a helicopter (Ingenuity, Balaram et al., 2021) on the surface of Mars. Soon, Martian samples will be returned to Earth for analysis ultimately followed by crewed missions to Mars. One of the major concerns for long-term Mars exploration missions is the possible detriment to the crew's health or spacecraft systems due to space radiation effects. Potential detrimental radiation effects on astronauts include chronic (stochastic) effects such as increasing the probability of developing cancer, or acute (deterministic) effects such as causing cataracts, cardiovascular, or neurological disorders (Cucinotta et al., 2001; Huff & Cucinotta, 2009). Space radiation can also affect electronics through cumulative damage or transient effects. The energetic electrons and protons deposit energy via ionization or atomic displacements in the materials of sensitive components, causing direct degradation, generating noise, or resulting in upsets (Dilillo et al., 2018). Hence, avoiding radiation-induced damage to biological systems or electronics is one of the biggest motivations for understanding the radiation environment on Mars.

Space radiation comes from three primary sources. First, galactic cosmic rays (GCRs) with energies typically >1 GeV/nucleon are created by supernovae (for nuclei with $Z < 30$) and neutron star mergers (for nuclei with $Z > 30$) throughout the galaxy (Drout et al., 2017). GCRs are mainly composed of protons and helium nuclei (~98%) while the remainder are heavy nuclei with similar elemental abundance as found in the solar system (Mewaldt, 1994). As the protons and nuclei are ejected from supernovae, they are accelerated by shock waves and traverse the interstellar medium. As the GCRs propagate through the galaxy, they interact by fragmentation of heavy nuclei, ionization energy loss and transmutation of radioactive nuclei. Once the GCRs enter the solar system, they are affected by the sun's magnetic field. The low-energy GCRs are shielded according to the strength of the sun's magnetic field which causes a periodic modulation. This solar modulation is often described as the electric potential that represents the energy loss of a GCR as it crosses the heliosphere into the Solar System (Wiedenbeck et al., 2007). Other changes in the intensity of GCR can be due to Forbush decreases. They consist of rapid decreases in the GCR intensity followed by a slow recovery when CMEs travel through interplanetary space (Guo et al., 2018). The second source of radiation comes from the sun itself. The sun's behavior varies with a ~11-year cycle between periods of high activity (solar maximum) and low activity (solar minimum). During solar maximum, the sun's increased activity generates many events (e.g., visible sunspots, coronal mass ejections, or solar flares) that emit solar energetic particles (SEPs). The protons (and heavier ions) are accelerated by the magnetic fields created in sunspots (short duration impulsive flares) or in coronal shock waves (long-lasting). The SEPs from the sun move along the interplanetary magnetic field lines (Lario, 2005; Nelson, 2016),—the so-called Parker spiral. Lastly, the third source of radiation applies to planets that possess intrinsic magnetic fields, such as Earth or Jupiter. The planetary magnetic field traps energetic charged particles (electrons, protons, and heavier ions) in a toroidal-shaped region around the planet (Jun et al., 2019). In the case of Mars, since it does not have an intrinsic magnetic field, there is no trapped radiation in its vicinity (O'Gallagher & Simpson, 1965).

The atmosphere of Mars is very thin compared to Earth's. The average atmospheric density at the surface of Mars is 0.016 kg/m^3 while for Earth it is 1.2 kg/m^3 (i.e., Mars' atmosphere is ~1% of Earth's) (Alexander, 2001). The incoming charged particles interact with the nuclei of the atmosphere via nuclear reactions and create a cascade of particles that eventually reach the surface (Feldman et al., 2002). Surviving GCRs and secondary particles can even reach the subsurface and interact with regolith nuclei. Additional neutrons can be generated within the subsurface that will eventually scatter (e.g., inelastic and elastic scattering) and be captured or escape back to the atmosphere. Figure 1 illustrates the interactions between the primary particles (e.g., a GCR ion) and the Martian surface that create secondary particles—among the secondaries are charged particles, gamma rays, and neutrons.

The Radiation Assessment Detector (RAD) onboard the MSL Curiosity Rover has been characterizing the Martian radiation environment since 2012. RAD instrument measures charged particle fluxes for given energy intervals. The RAD instrument also generates linear energy transfer (LET) and energy deposition (dose) histograms in silicon and plastic (tissue equivalent). The dose and the LET spectrum are commonly used to define the risk from ionizing and non-ionizing radiation (Hassler et al., 2012). Additionally, the High Energy Neutron Detector (HEND) onboard the 2001 Mars Odyssey spacecraft has been measuring the neutron albedo from orbit since 2001 (Boynton et al., 2004).

Models and simulations often complement these in-situ measurements. Accurate models and tools can help predict risk, design instruments, and validate current measurement techniques. In a major effort to validate the different predictive models (i.e., various available radiation transport tools), a group of several international teams simulated GCRs transport through the Martian atmosphere and compared the results with the actual, in-situ RAD measurements. This exercise revealed how sensitive the models were to different physical variables (i.e., atmosphere conditions, regolith composition, interaction cross section libraries, etc.) and on how difficult it was to predict the radiation environment on the surface of Mars. Critically, the RAD analyses looking at the dose equivalent estimates demonstrated the importance of the neutron contribution to the total dose equivalent at the surface (Matthiä et al., 2017).

Determining an accurate neutron dose is complex because it depends on the neutron's energy, the number of neutrons, and the target material. Neutrons deposit their energy by nuclear interaction, resulting in secondary gamma rays, protons, alpha particles, and heavier nuclear fragments that can lead to significant ionization in a material. The radiobiological response of the neutrons is highly dependent on the neutron energy (Stricklin et al., 2021). While neutrons with energies between 0.5 and 50 MeV correspond to a higher severity of the biological damage (Cool & Peterson, 1991), neutrons of all energies will contribute to the total radiation hazard. Thus,
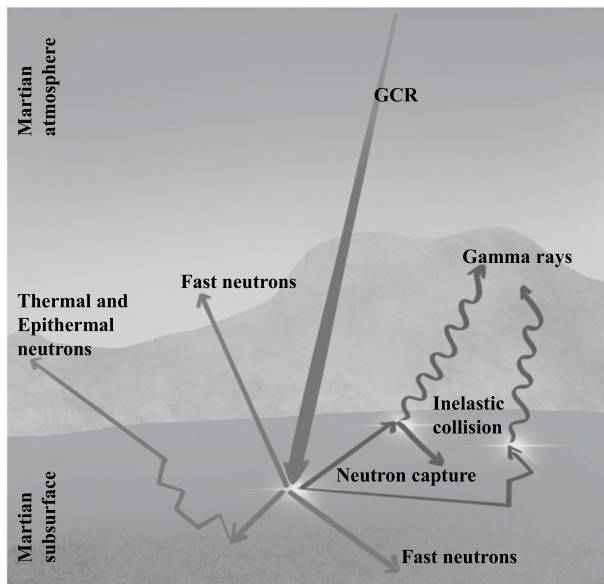
Figure 1. Schematic of a galactic cosmic ray (GCR) traversing the Martian atmosphere and subsurface. GCRs interact with the nuclei of the regolith creating secondary particles; these include neutrons that continue to scatter creating a neutron albedo field with a full range of energies and generate gamma rays depending on the interaction. Each interaction happening in the subsurface is represented by a flash point in the diagram. Other cascade interactions that happened in the atmosphere are not presented in the illustration. After the neutrons interact in the surface nuclei, they are moderated and can leave the surface.

knowing the comprehensive neutron flux over a wide energy range will allow us to determine a more accurate neutron dose at the surface of Mars and help to validate our modeling and processing efforts.

To determine the surface neutron dose, this paper is composed as follows. Section 2 describes the two instruments that provided the data for this study. Section 3 presents our proposed inversion methodology to obtain the surface neutron flux spectra from the orbital neutron measurements for selected atmospheric environmental conditions. Because one of the measurements was taken from orbit, we will derive the surface flux spectra by accounting for atmospheric attenuation based on a series of extensive Monte Carlo simulations. Results and analyses for the thus-obtained surface neutron spectra and doses are presented in Section 4. Finally, Section 5 summarizes our findings and their implications.

2. Instruments Overview and Measurements

HEND and RAD, the two instruments selected for this study, measure Martian neutrons from different perspectives. The main differences between the instruments are described in Table 1. We describe their design, performance, and data products in this section.

2.1. 2001 Mars Odyssey—HEND Instrument

The HEND instrument is onboard the 2001 Mars Odyssey spacecraft. The spacecraft orbits Mars at an altitude of ∼400 km every 2 hr. For the past two decades, HEND has mainly measured the neutrons produced by the Martian surface when the GCRs interact with the nuclei in the atmosphere/surface materials. Of the secondary particles created, the neutrons leaking from the surface are often called albedo neutrons (Drake et al., 1988; Reedy & Arnold, 1972). Albedo neutrons, after traversing the atmosphere, eventually reach orbit and are detected by HEND in the Mars Odyssey orbit. The instrument consists of five different detectors: three ^{3}He proportional counters and two scintillators as can be seen in the diagram on the left of Figure 2. Polyethylene moderators of different thicknesses surround each proportional counter, and the detectors are named after the amount of moderator around each sensor. The detectors are labeled Small Detector (SD), Medium Detector (MD), and Large Detector (LD). The moderator thickness also determines the sensitive energy range for each counter: SD from 0.4 eV to 1 keV, MD from 0.4 eV to 100 KeV, and LD from 10 eV to 1 MeV. Additional Cd shields cover the He-3 detectors to filter out low energy ($E_n < 0.4$ eV) neutrons. The internal scintillator (SC/IN) is made of stilbene crystal, while the external scintillator (SC/OUT) is CsI. Together, they detect neutrons from 800 keV to 15 MeV and gamma rays from 60 keV to 2 MeV (Boynton et al., 2004).

The Lunar and Planetary Laboratory (LPL) team of the University of Arizona provided the HEND data (20 years of data) used in this study. The data set contains spacecraft location, time stamps, measurements for each detector (SD, MD, LD, SC/IN, and SC/OUT), background measurements for each detector, and a flag that marks intervals of known SEP events. Mars' surface neutrons contain information from the subsurface hydrogen content. Therefore, the total counts detected by HEND on orbit are the combined signal from Mars and neutrons produced in the spacecraft by GCRs. To estimate the spacecraft's induced background neutrons, HEND took measurements during cruise and aerobraking. First, the measured signal was produced on the spacecraft by GCR protons and then corrected by the solid angle of Mars (for cruise and elliptical orbit). Over the course of the mission, the stilbene scintillator—that looks to open space- and the anticoincidence shield record the background neutron noise generated in the spacecraft itself by the GCRs (Mitrofanov et al., 2002). We removed this noise from the count rate measurements used in this study. To obtain the neutron flux at the surface, we will use only the neutrons escaping Mars's surface. In Section 3.1, we will explain the methodology used to extract the surface-neutron flux spectra from the orbital HEND measurements.

Table 1
High Energy Neutron Detector and Radiation Assessment Detector Properties Comparisons

	HEND	RAD
Location	Sun-synchronous polar orbit of 400 km of altitude and 93.1 degrees of inclination	Surface of Mars at Gale Crater located in the south hemisphere, featuring Mount Sharp
Detector type for neutral particles	He-3 proportional chambers and scintillators	Scintillators with different densities and compositions, with additional anti-coincidence shield
Neutron energy sensitivity	Low energy, $<\sim$10 MeV	High energy, $>\sim$6 MeV
Additional measurements	Solar activity, surface hydrogen content	Charged particle spectra, dose rate, histogram of Linear Energy Transfer
Field of view—footprint	Orbital Mapping—400 km orbit, coverage 600 × 600 km.	Surface observations $\sim$10 s around the rover
Directionality	Omnidirectional (from horizon to horizon)	Omnidirectional neutrons coming both from the atmosphere and the regolith

2.2. Mars Science Laboratory—RAD Instrument

The RAD instrument is part of the payload of the MSL rover, which has been on the surface of Mars for the past 10 years. RAD monitors both spectra and doses from charged and neutral particles coming directly from the GCRs, SEP, and their interactions with the atmosphere. To accomplish this, RAD uses a charged-particle analyzer using multiple particle detector types to identify and count different particle species with a wide range of energies. A vertical stack of three solid-state silicon detectors of 300 μm thickness makes up each particle telescope component at the top of the instrument (detectors A, B, and C). The scintillation block is located at the end of the particle telescope and consists of a CsI crystal scintillator (detector D) and a tissue-equivalent organic plastic scintillator (detector E). The anti-coincidence shield (detector F) is made of a plastic scintillator and surrounds both detectors D and E (Hassler et al., 2012). The right panel in Figure 2 shows a diagram of the configuration of RAD's detectors.

The Multi-Mission Radioisotope Thermal Generator (MMRTG) powers the MSL rover by using the heat produced by the Pu-238 radioactive decay. As Pu-238 decays, neutrons are created by spontaneous fission and (n, α) reactions with the fuel. The peak energy of these neutrons lies between 4 and 5 MeV (Jun et al., 2013). Because the neutrons created by the MMRTG can potentially contaminate the RAD neutral particle measurements, the low energy threshold for detectors D and E were set to be 20 and 6 MeV, respectively. The difference in densities of detectors D ($\rho = 4.51$ g/cm^3) and E ($\rho = 0.97$ g/cm^3) and their different composition allows the instrument to distinguish between neutrons and gamma rays. Detector D stops most high-energy gamma rays while neutrons interact with the hydrogen atoms and are slowed down in detector E (Köhler et al., 2014). However, both detectors are to various degrees sensitive to both gamma rays and neutrons. When analyzing the RAD data, there are additional sources of noise in the RAD data that need to be filtered. The first occurs while the instrument is communicating with the rover's computers. The second comes when DAN's pulsed neutron generator (PNG) is actively firing; The PNG emits 14 MeV neutrons at different intervals, and as the neutrons interact with the regolith, they are emitted back (albedo). Dynamic Albedo Neutron (DAN) records the time profile of the thermal and epithermal neutrons to estimate the hydrogen content (Zeitlin et al., 2016).

The onboard electronics prioritizes RAD data from priority levels of 0–3 according to the frequency of the biological-damaging events recorded. Priority 2 and 3 are used for rare events, while priorities 0 and 1 are for more common events—the memory stores a certain number of events for each priority. When the memory fills up, no more events are recorded, and a counter keeps track of the number of events being missed. To correct the downloaded data on the ground in post-processing, the RAD team scales the data by a factor that is equal to the number of physical events divided by the number of events measured (i.e., factor >1 and is defined as factor = [#occurred]/[# recorded]), where [#occurred] = [#recorded] + [#missed] (Zeitlin et al., 2016).

Note that before sol ∼1,100 (2015-05-30 UTC—coordinated universal time), the neutral particle events were double-counted as priority 0, and the scaling factor needs to be corrected for that. Since then, the issue was fixed, so that no additional corrections were needed to interpret the data (Zeitlin et al., 2016). Nevertheless, we limited the data set used in this study to sols 1,200–2,000 to avoid adding more corrections.

The Planetary Data Science (PDS) servers host the archives for the MSL—RAD measurements. The files can be downloaded for any period during the mission, and each file contains the observations performed during a particular sol. Each observation includes header notes, housekeeping data, counter data, histogram data, and event pulse-height records. The D and E energy deposition histograms provide sums of energy deposited in each bin for each detector, produced both from neutrons and gamma rays. The methodology used to analyze the RAD histograms to obtain a neutron flux will be presented in Section 3.2.

3. HEND and RAD Data Processing

Although the HEND and RAD instruments are sensitive to the neutrons coming from the Martian surface, the nature of the data is very different as presented in Table 1. Neither instrument can provide a direct measurement of the neutron flux energy spectrum from the surface. HEND measures the neutrons reaching orbit from Mars' surface and RAD detects the energy deposition from neutrons and gamma rays interacting with both D and E detectors coming from the area around the rover. Each instrument has a
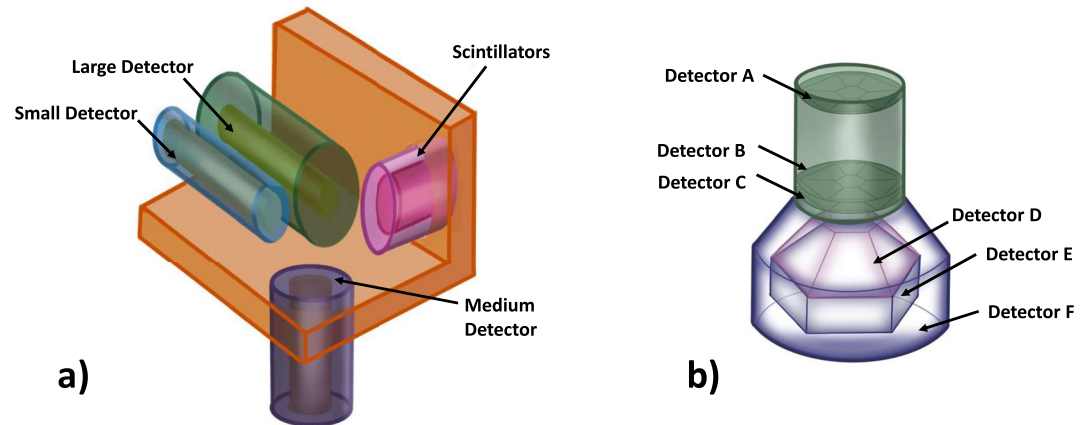
Figure 2. (a) High Energy Neutron Detector instrument illustration showing the structure in orange and the He-3 detectors with moderator material for Small Detector (blue), Medium Detector (violet), Large Detector (green), and scintillation block (magenta). (b) Illustration of Radiation Assessment Detector instrument schematic displaying the solid-state detectors A, B, C, the Crystal scintillator D, tissue equivalent scintillator E, and the anti-coincidence shield F (right). Not to scale.

different footprint as described in Table 1, HEND observes areas of 600×600 km, while RAD is sensitive to the environment coming from a few 10 s of meters around the MSL rover. Because we want to understand the long-term trend, the spatial coverage of the instruments does not alter our methodology, instead we average the data over long periods. Both data sets are calibrated and cleaned to remove extraneous noise sources. The data on both instruments are also sensitive to solar energetic proton events reaching Mars. The contributions from these events are also removed in this study.

The challenge is to develop a methodology to use the HEND and RAD data together to study the whole energy range of the neutron component on Mars caused by the background GCRs radiation. The block diagram in Figure 3 represents the methodology we use in this study. We start with the assumption that the neutron differential flux will follow a power law fit of the form $f(E) = I E^{-S}$, where E is the energy of the neutrons, I is the
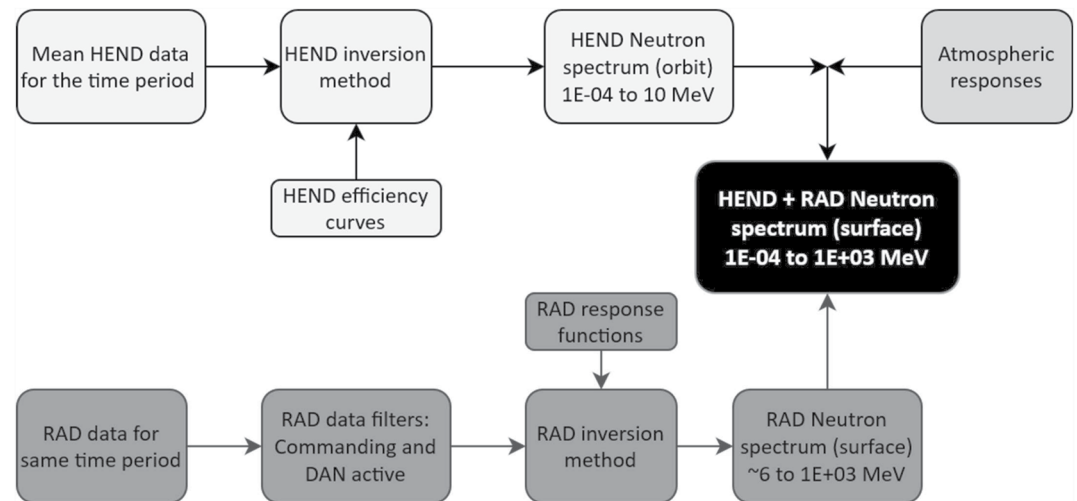
Figure 3. The block diagram represents the methodology used in this analysis. Starting with the High Energy Neutron Detector (HEND) data, the power law inversion method is applied and convoluted with the efficiency curves to obtain the orbital neutron spectrum (orange block flow shows the HEND-derived neutron flux inversion method). Then, using the atmospheric (blue block) responses for neutrons at different energies, the neutron flux at the surface can be derived from the orbital neutron flux. Similarly, a similar power law inversion method is used to determine the neutron flux spectra using the Radiation Assessment Detector (RAD) response functions and the RAD data (Yellow block flow shows the RAD method to determine neutron flux). Finally, because the neutron flux at the surface, derived from HEND and RAD, covers different energy ranges, we can unfold a wide neutron energy range by combining both.

Start with a range of values for *I* and *s* (vary)

$$f(E) = I_{orbit}E^{-s}$$

X

SD response function
MD response function
LD response function

→

Simulated counts for HEND

SD'
MD'
LD'

Find the best minimum square difference of all the *I* and *s*

⇄

Measurements from HEND

SD
MD
LD

Applied the atmospheric correction factors from the MCNP6 simulations
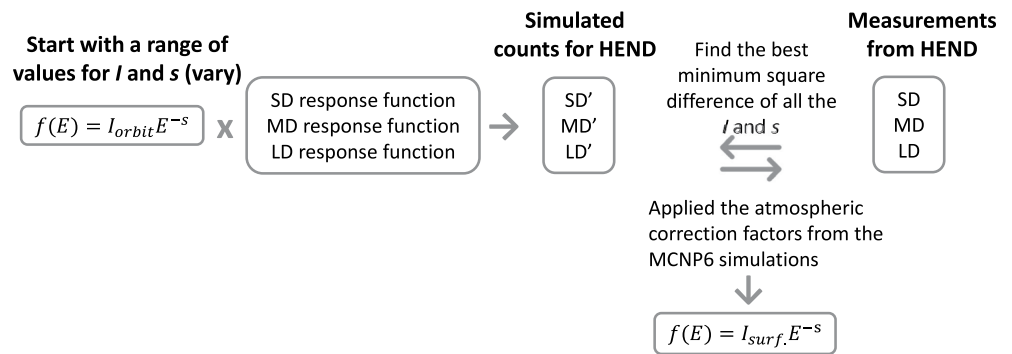
↓

$$f(E) = I_{surf}.E^{-s}$$

Figure 4. The block diagram shows the methodology to obtain the neutron flux fitted to the High Energy Neutron Detector measurements. First, we assumed a power law-shaped flux. Then the calculated flux is multiplied by the response functions for each detector to determine the calculated counts for SD', MD', and LD'. Next, the calculated counts are compared with measurement averages over time. Finally, the best fit is found by varying the values of I and S until the difference between SD, MD, Large Detector, and SD', MD', LD' is minimum.

differential intensity of the power-law spectrum (typically in units of neutrons/s-cm^2-eV or neutrons/s-cm^2-MeV) and S is the spectral index. The general shape of the neutron spectrum follows a $1/E$ for a non-absorbing medium. Historically, the neutron energy spectrum has been calculated in three energy regimes or groups: thermal (<1 eV), epithermal (1 eV–1 MeV) and fast ($E > 1$ MeV). There is typically an increase around 1 MeV known as the "knee" and it corresponds to the evaporation neutrons from spallation interactions. The high energy portion will follow similar power-law distribution shape as the incident GCRs with different intensities (Hess et al., 1959). To cover a wide energy range (1 eV–100 MeV) we will implement the data fit in two separate energy ranges: (a) Using HEND data we can fit neutrons with $E < 10$ MeV, and (b) RAD data fits for neutrons with $E > 6$ MeV.

The next step is to determine the neutron count rates from the HEND orbital data. The corresponding neutron counts on the surface of Mars are found after applying a correction factor to account for atmospheric attenuation at each location of the Curiosity rover and by applying the HEND's efficiency curves. To find the coefficients that best fit the power law neutron flux for the HEND orbital data, we then implement a least squares fitting routine (Weisstein, 2002). This method consists of finding the coefficients that minimize the sum of the squared offsets of the fits to the data. In parallel, the same process is applied to RAD data obtained during the same time intervals over which HEND measurements are made.

By combining the HEND and RAD surface power law neutron fluxes, we can approximate a full energy spectrum (10 eV < energy <1 GeV) on the surface of Mars. Sections 3.1 and 3.2 describe in more detail the data processing, assumptions, and methodologies for each data set. The HEND and RAD data were selected for periods where both instruments have simultaneous observations and when the MSL rover had spent more than five sols in the same location. The data is averaged for each period, averaging possible effects due to atmospheric changes, topography, and local time variations.

3.1. HEND Power Law Fit and Atmospheric Transfer Function Methodologies

The process we developed to obtain the orbital neutron flux from HEND measurements is described in Figure 4. We start by assuming the neutron differential fluxes follow $f(E) = IE^{-S}$, where I is the differential intensity I in units of [#/MeV s cm^2], and S is the spectral index. Next, we find the intensity and spectral index that best describes the given data interval using the response functions for each detector as extracted from previous literature (Litvak et al., 2020). Using the least squares fitting method, we were able to find the corresponding I and S that best fit the power law flux spectrum.

Neutrons leaking from the surface must traverse the atmosphere to reach orbit and be detected by HEND. Because we are using data accumulated over five or more sols, we are averaging the influence of the spacecraft location or local variations. We averaged the neutrons counts for each detector during the selected periods. The atmospheric conditions need to be accounted for to determine the initial neutron flux from the surface that creates the respective HEND measurements. To understand how the atmosphere's density influences neutron transport, we performed a series of Monte Carlo simulations with the MCNP6 radiation transport code (Pelowitz, 2013).
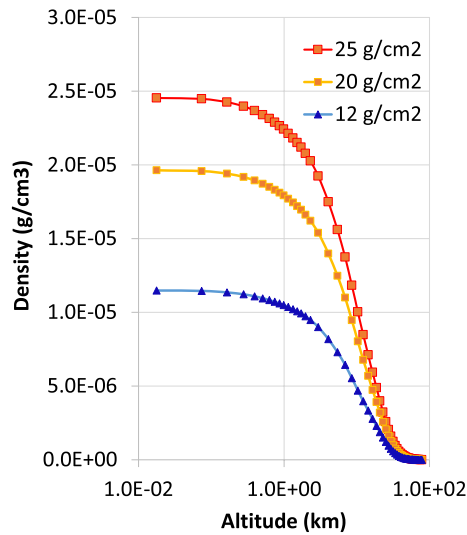
Figure 5. The atmospheric density in our simulation follows the same formulation from Jun et al. (2013) based on the MarsGRAM (Justh & Justus, 2007). The atmospheric density varies widely through the Martian seasons. The density definition for the MCNP6 simulations varied between 12 and 25 g/cm² in increments of 1 g/cm². Here, only three atmospheric values of 12, 20, and 25 g/cm² densities are plotted to show the change as a function of altitude.

The simulation setup started with the GCR source derived for the solar modulation (as measured on Earth), Next the atmosphere was modeled as a cylinder of 5×10^4 km in diameter with a height of 425 km. The geometry was modeled with 20 m of Martian subsurface and the atmosphere split into 50 layers with different densities according to calculations of Mars' atmosphere as illustrated in Figure 5. The total atmospheric areal densities for each simulation were between 12 and 25 g/cm². The atmosphere was modeled using a representative composition of the Martian atmosphere with ~27% carbon, ~70% oxygen, ~1.1% nitrogen, ~1.4% argon, and traces of hydrogen (Jun et al., 2013). The subsurface layers had a 1.8 g/cm³ density, and the composition was representative of Mars. Hydrogen and chlorine content are carefully modeled for each location—the neutron energy distribution and intensity are strongly dependent on the H and Cl content. Hydrogen nuclides are efficient in slowing down neutrons, while chlorine nuclides absorb low-energy neutrons efficiently. Commonly, the H concentration is converted into water equivalent hydrogen (WEH). Similarly, the absorption equivalent chlorine (AEC) content represents the effects from Cl and other neutron absorbers atoms like Fe and Si. Based on the simulations results, we estimated the energy-dependent neutron attenuation factor for different areal atmospheric densities. Based on the results of the simulations, we estimated the energy-dependent neutron attenuation factor for different areal atmospheric densities. These atmospheric factors and subsurface models transform the HEND-orbit counts into HEND-surface counts. The resulting values of the intensities and spectral index coefficients for the HEND-orbit and HEND-surface data are presented in Section 4.

3.2. RAD Power Law Fit Methodology

Initially, we created a routine to gather the raw RAD histograms recorded by the detectors D and E. To determine the average energy distribution of the neutral particles, we calculate the cumulative histogram and then divide it by the observation time. Typically, one sol corresponds to ~87 observations of 16 min each. As an example, the cumulative histograms of detectors D and E for all measurements made during sols 1,221–1,243 are presented in Figure 6.

Since the D and E detectors are each sensitive to both neutrons and gamma rays, the next step is to find the corresponding fluxes on the surface of Mars that would produce the same count rates as measured by RAD for a given period. Like the HEND data processing, we again assume that the neutron and gamma ray differential fluxes will follow a power law fit as a function of energy (E) of the form $f(E) = I E^{-S}$ where I is the differential intensity I in units of [#/MeV s cm²], and s is the spectral index. I and S are the coefficients we need to fit for neutrons (I_n and S_n) and gamma rays (I_γ and S_γ).

The procedure we follow is based on an inversion method, similar to the one presented by Guo, Zeitlin, et al. (2017); The detector response function (DRF) matrix for detector D or E gives the probability that an incident particle (neutron or gamma ray) with specific energy (16 bins each) will deposit a fraction of its energy in D (19 energy bins) or E detector (21 energy bins) within a particular energy interval. The RAD team shared with the DRFs (J. Guo, personal communication, 26 January 2021) via internal communication. We calculate the predicted histograms assuming a wide range of values for I_n, S_n, I_γ, and S_γ. The convolution of the neutron and gamma rays' flux spectra with the DRFs following the matrix formulation as described in Figure 7 results in a derived histogram for each detector. The least squared fitting method is applied by comparing the expected histograms with the measured histograms to find the best approximation for I and S (for neutrons and γ). The next section presents the results of the matrix inversion methodology for the RAD data to find the neutron flux coefficients.

4. Results

In this section, we describe the results for fifteen MSL locations selected between sols 1,220 and 2,000. We chose locations where the MSL rover spent more than 5 sols in the same location to limit the effects of geological and topographical variations and focus on the environmental variations. The selected intervals covered ~700 sols, enough to provide seasonal sampling—one Martian year is 668 sols.

a)

b)
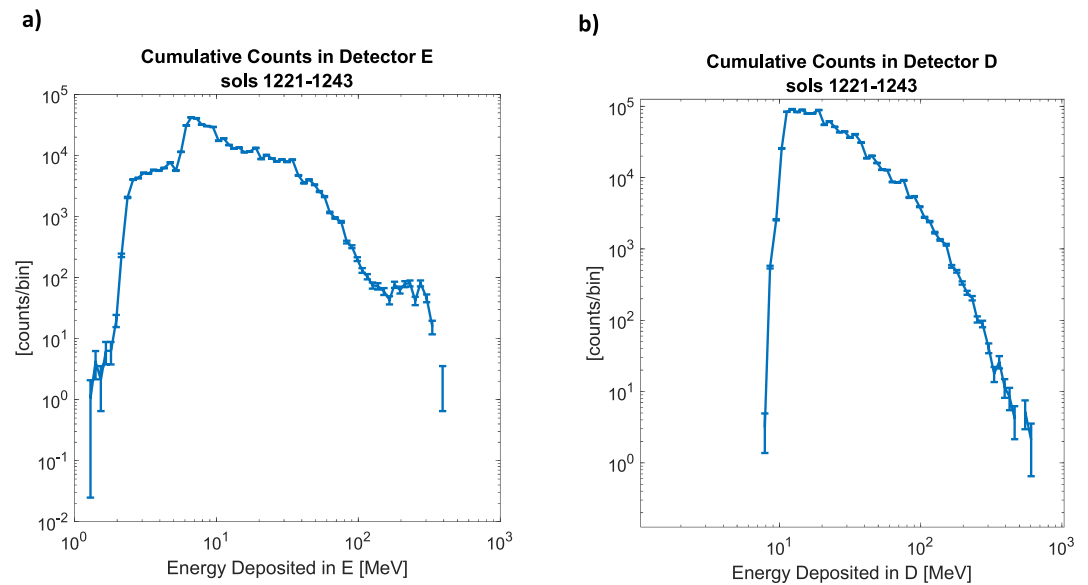
Figure 6. Cumulative measured histograms of energy deposited in detectors E (left panel) and D (right panel). Histograms are shown with 96 energy bins in this example. Later modification required re-binning to match the number of bins from the detector response functions.

4.1. Neutron Spectrum From Power Law Inversion

Table 2 presents the results for RAD and HEND data for which we obtained estimates of the intensity (I in units of [#/MeV s cm^2]) and the spectral index (S) for the neutron flux using the described methodologies in Sections 3.1 and 3.2.

$$f = I E^{-s} \tag{1}$$
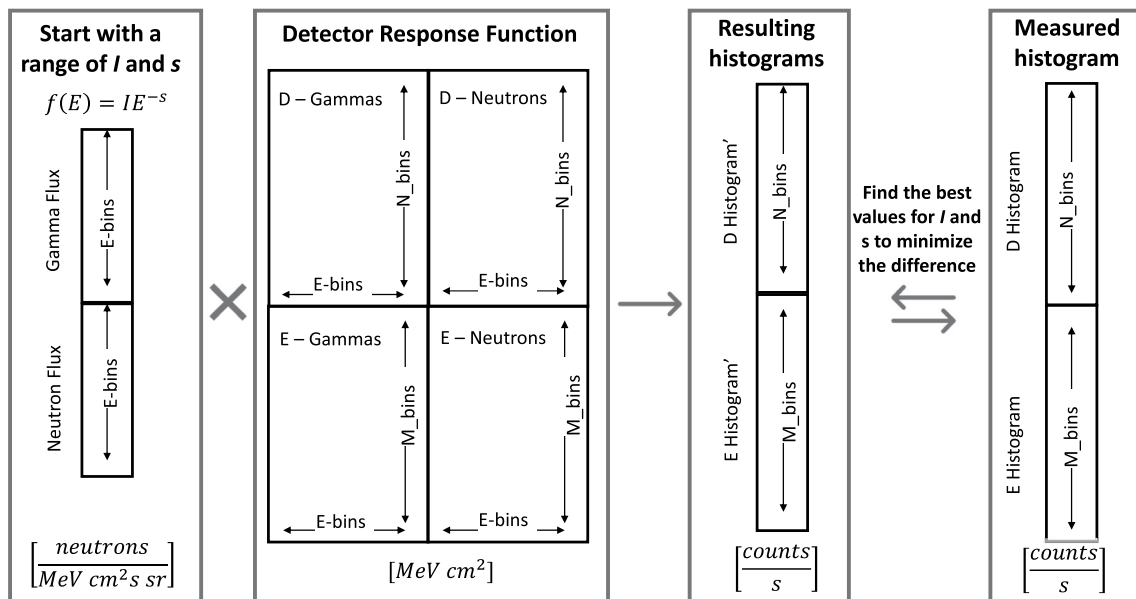
Figure 7. Matrix diagram showing the Radiation Assessment Detector (RAD) formulation from the measured histogram and the defined detector response functions (DRFs) to obtain the gamma ray and neutron fluxes. The best guess of the neutron flux spectra for a given period results when the difference between the modeled and measured histogram is minimum. The measured histograms for detectors D and E are obtained from the RAD Planetary Data Science data set. The estimated histograms are obtained by multiplying the assumed neutron flux spectra with the detector response function (Histogram = DRF × flux).

Table 2
High Energy Neutron Detector (HEND) and Radiation Assessment Detector (RAD) Power Law Fit Results for the Locations Selected, Including the Columns for the Start and Stop Sols of the Intervals, Solar Longitude (L_s Representative of the Martian Season), and Results for RAD, HEND in Orbit, and HEND Projected to the Surface

Date	Sol_{start}	Sol_{stop}	L_s	Solar modulation	RAD I_n [# / MeV s cm²]	RAD S_n	HEND orbit I_n [# / MeV s cm²]	HEND orbit S_n	HEND surf. I_n [# / MeV s cm²]	HEND surf. S_n	Effective dose (uSv/day)	Dose equivalent (uSv/day)
01/12/16	1,221	1,243	94	500	0.168 ± 0.02	0.619 ± 0.14	0.154 ± 0.02	0.928 ± 0.15	0.346 ± 0.1	1.076 ± 0.08	143 ± 11.8	136 ± 7.9
04/19/16	1,317	1,329	146	468	0.143 ± 0.02	0.599 ± 0.14	0.154 ± 0.02	0.941 ± 0.14	0.339 ± 0.1	1.05 ± 0.1	133 ± 6.6	123 ± 5.1
05/02/16	1,329	1,342	153	464	0.151 ± 0.02	0.608 ± 0.14	0.155 ± 0.02	0.942 ± 0.14	0.347 ± 0.1	1.048 ± 0.1	135 ± 6.7	125 ± 5.2
05/30/16	1,357	1,369	161	450	0.152 ± 0.02	0.609 ± 0.15	0.155 ± 0.02	0.946 ± 0.14	0.35 ± 0.1	1.055 ± 0.1	136 ± 7	127 ± 5.3
06/30/16	1,387	1,398	184	447	0.155 ± 0.02	0.601 ± 0.12	0.155 ± 0.02	0.942 ± 0.14	0.35 ± 0.1	1.053 ± 0.1	143 ± 6.3	131 ± 5
07/31/16	1,417	1,427	202	464	0.153 ± 0.02	0.615 ± 0.14	0.155 ± 0.02	0.941 ± 0.14	0.339 ± 0.1	1.049 ± 0.1	132 ± 6.6	124 ± 5.2
09/08/16	1,455	1,468	219	436	0.144 ± 0.02	0.621 ± 0.14	0.155 ± 0.02	0.936 ± 0.14	0.344 ± 0.1	1.052 ± 0.11	124 ± 6	119 ± 5.1
10/13/16	1,489	1,499	241	407	0.162 ± 0.02	0.62 ± 0.15	0.156 ± 0.02	0.923 ± 0.14	0.354 ± 0.1	1.063 ± 0.12	138 ± 7	131 ± 5.4
11/20/16	1,526	1,553	282	385	0.162 ± 0.02	0.617 ± 0.15	0.156 ± 0.02	0.926 ± 0.14	0.354 ± 0.1	1.064 ± 0.12	140 ± 7.2	132 ± 5.5
12/20/16	1,555	1,571	294	386	0.168 ± 0.02	0.616 ± 0.14	0.156 ± 0.02	0.928 ± 0.14	0.353 ± 0.1	1.055 ± 0.12	144 ± 7.3	133 ± 5.5
02/22/17	1,617	1,628	328	357	0.157 ± 0.02	0.607 ± 0.15	0.156 ± 0.02	0.94 ± 0.14	0.344 ± 0.1	1.052 ± 0.1	140 ± 7.2	129 ± 5.3
03/25/17	1,648	1,659	345	348	0.159 ± 0.02	0.611 ± 0.15	0.158 ± 0.03	0.938 ± 0.13	0.355 ± 0.09	1.073 ± 0.11	141 ± 7.3	135 ± 5.4
05/25/17	1,707	1,711	10	359	0.156 ± 0.02	0.598 ± 0.14	0.162 ± 0.03	0.931 ± 0.13	0.361 ± 0.09	1.094 ± 0.1	147 ± 7	143 ± 5.3
06/29/17	1,741	1,746	26	350	0.17 ± 0.02	0.619 ± 0.15	0.158 ± 0.03	0.941 ± 0.13	0.358 ± 0.09	1.08 ± 0.11	145 ± 10.5	140 ± 7
07/12/17	1,754	1,781	45	383	0.161 ± 0.02	0.60 ± 0.13	0.155 ± 0.02	0.942 ± 0.14	0.354 ± 0.1	1.072 ± 0.11	149 ± 6.8	138 ± 5.2
10/19/17	1,850	1,864	82	405	0.159 ± 0.02	0.606 ± 0.15	0.155 ± 0.02	0.936 ± 0.14	0.35 ± 0.1	1.068 ± 0.11	143 ± 7.4	134 ± 5.6
11/16/17	1,877	1,887	93	367	0.159 ± 0.02	0.605 ± 0.15	0.156 ± 0.02	0.94 ± 0.14	0.353 ± 0.1	1.062 ± 0.11	144 ± 7.3	134 ± 5.4

Note. The calculated fluxes intensity, I, are omnidirectional fluxes integrated over all directions.
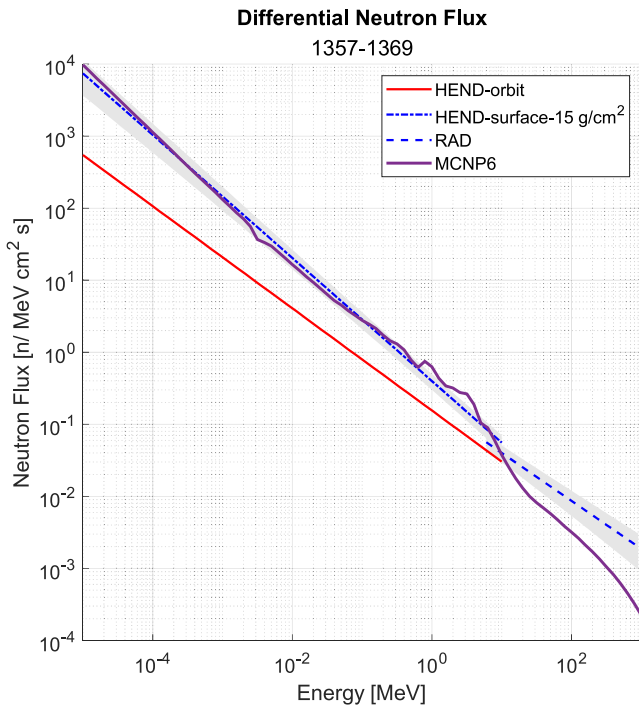
Figure 8. Summary plot of the neutron fluxes from combining Radiation Assessment Detector (RAD) and High Energy Neutron Detector data power law approximations for sols 1,357–1,369. The red line is the differential neutron flux derived from HEND-orbit data. The dotted blue line is the surface differential neutron flux after the respective atmospheric correction for the HEND-orbit flux during that sol period. The dashed blue line is the surface differential neutron flux derived from the RAD data. The shaded gray bands are the error bar (standard deviation) from the power law fits from HEND-surface and RAD data. The purple solid line represents the differential neutron flux from the MCNP6 simulations using the initial conditions for the sol period including the galactic cosmic ray intensity source (solar modulation), atmospheric density, water, and chlorine content in the soil. See Supporting Information S1 and Table 2 included parameters for all locations.

We obtained the power law flux spectra (Equation 1) with the values in Table 2. Then, we combined the RAD and HEND-surface spectra to determine the total neutron spectrum that covers energies between 10 eV and 1 GeV. The statistical uncertainty of the neutron flux spectra follows the propagation of σI and σs, as shown in Equation 2.

$$\sigma f = (I E^{-s}) \sqrt{\frac{\sigma I^2}{I^2} + (\ln(E) \cdot \sigma s)^2} \tag{2}$$

Figure 8 shows the plot for the entire energy range for the interval between sols 1,221–1,243. Once the HEND data are corrected for the atmospheric attenuation, the surface equivalent fluxes, as seen in blue in Figure 8, are higher than the HEND-orbit fluxes (in red). The fluxes derived from RAD data and HEND-surface data intercept around 6–10 MeV, which supports our expectation of creating a continuous neutron flux. To validate the neutron fluxes estimated using the power law fits and atmospheric correction, we performed a series of MCNP6 simulations. Each simulation used as input the GCRs intensity based on the actual solar modulation at the time (Burger, 2000), atmospheric density derived by the Rover Environmental Suite instrument (REMS) on MSL (Gómez-Elvira et al., 2012), and the soil at each location is modeled based in the average bulk composition from Mars Exploration Rover APXS (alpha particle x-ray spectrometer) (McSween & Huss, 2010) and derived hydrogen and chlorine content measurements taken by the DAN instrument (Mitrofanov et al., 2012). The simulations considered the transport of GCRs into the atmosphere and soil of Mars. Nonetheless there are details such as topography, elevation, and other real-life parameters that are not accounted for in the simulations. The next section looks at the trends of the neutron fluxes over time in more quantitative detail.

4.2. Neutron Flux Trends

Any temporal variations of the neutron fluxes are difficult to identify in the plot like Figure 8 and at other locations (though not shown in this paper). In this section, we look at the neutron flux behavior at energies of 1.0E−04, 1.0E−01, 11, and 20 MeV. We estimate the differential neutron flux at each selected energy from the differential fluxes defined for each location (using the coefficients from Table 2). The HEND-surface flux was used for 100 eV and 100 keV, while the RAD flux was used for 11 and 20 MeV. Variations of the differential neutron fluxes at each energy can be seen more clearly in the top four panels of both plots in Figure 9. The seasonal variation of the atmospheric total column mass/area is also included in the last panel of Figure 9 for comparison purposes using REMS data. The atmospheric surface pressure data (column mass over an area at the surface) is presented as a band that corresponds to the range covered for maximum and minimum data recorded over time (i.e., the atmospheric surface pressure varies throughout the sol). The vertical dotted lines in all the plots of Figure 9 represent the start of each Martian season as defined by the solar longitude (L_S). The error bars in Figure 9 are larger than the variations of the neutron flux magnitude as a function of sol.

Two prominent features of Figure 9a are a decrease in high energy neutron flux (from RAD) around sol 1,455 and an increase in the low energy neutron flux (from HEND) around sol 1,770. The decrease of neutron fluxes at 1,455 corresponds to when the MSL rover was investigating the region around the Murray Buttes, a formation that stood about 5 m higher than the rover, and thus the neutron flux decrease is only present at energies derived from RAD data. These formations are created of sandstone that has eroded over time and provide shielding from the radiation at a given solid angle depending on the rover's positioning (Ehresmann et al., 2021; Guo et al., 2021). Simulations of the effects of topographic changes around the rover explain the variation of the neutron flux variations due to shielding effects to wall proximity (Dibb et al., 2019). The neutron flux enhancement ~sol 1,707
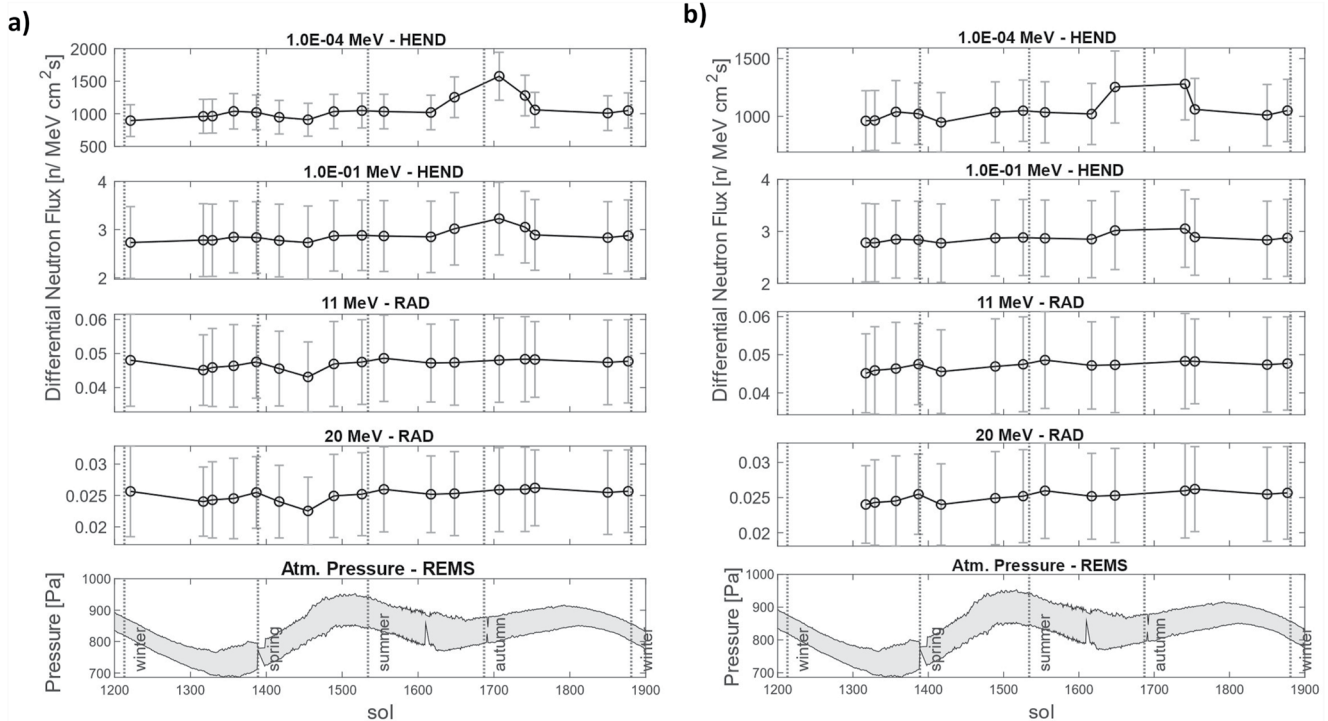
Figure 9. Time plots of the neutron fluxes for four selected energies as a function of sol. Top four plots on (a) and (b) are neutron fluxes at each selected energy (100 eV, 100 keV, 11 MeV, and 20 MeV). The bottom panel shows the atmospheric column mass/area as measured by Rover Environmental Suite instrument vs. sol. Panel (a) show the neutrons flux trends. Panel (b) presents the same data as panel (a) but we removed the data from sols 1,455 and 1,707 (see the text for the reason). The variation of the neutron flux from location to location is smaller than the error calculated for the neutron fluxes.

(∼5/25/2017) can be attributed to a medium-intensity solar flare (class C) that was detected by HEND but not by RAD (NOAA, 2017). The RAD measurements are sensitive to protons energetic enough to traverse the atmosphere. The solar proton event observed in this period was related to a class C (lower energy solar events). Therefore, the proton environment enhancement that occurred during the SPE did not reach the surface of Mars due to the Martian atmosphere attenuation. Additionally, we search for Forbush decreases in our selected data, and found that our first location (Sol 1,221) coincides with an event reported on 1 December 2016 (Forbush, 1938; Guo et al., 2018). To continue our analysis and keep the neutron flux independent of local environment variations, we removed the data from sols 1,221, 1,455, and 1,707, as seen in Figure 9b.

4.3. Neutron Dose Rates

In this section, we provide a summary of our neutron dose computation using the power-law fit developed in this study and compare them to a few neutron dose estimates from previous studies. Also, we present the temporal trend of neutron dose estimates in response to variations of the atmospheric density and the solar modulation parameter.

The amount of energy a radiation particle deposits per unit mass of material is called absorbed dose. Often, we need to estimate possible damage from absorbed dose to a biological system for different organs or tissues or for whole-body exposure, which is further dependent on the type of incident radiation and how much energy is deposited per unit length of the transit through the material (LET). Identifying the correct dose quantity can be confusing, and, in this study, we follow the definitions and equations from the International Commission on Radiological Protection (ICRP) (ICRP, 2010):

Absorbed dose, D (Gy = Joule/kg): energy deposited per unit mass where $D = dE/dm$

Dose equivalent, H (Sv): Absorbed dose times Q, the quality factor defined as a function of the LET for radiation in water where $H = DQ$

Table 3
Evolution of Dose Equivalent Rate From Previous and Current Studies

Dose equivalent rate	Neutron energies	Date interval	Method	Dose conversion	Reference
61 ± 15 μSv/d	~8–100 MeV	8/12/2012 to 08/12/2013	Neutron inversion flux from RAD data (1)	U.S. NRC, 10 CFR 20.1004	Kohler et al. (2014)
25.3 ± 3.3 μSv/d	~8–100 MeV	11/15/2015 to 01/15/2016	Neutron inversion flux from RAD data (2)	U.S. NRC, 10 CFR 20.1004	Guo, Zeitlin, et al. (2017)
200 μSv/d	1 MeV–10 GeV	11/15/2015 to 01/15/2016	Simulated with GEANT4—PLANETOCOSMICS	ICRP 60	Matthia et al. (2017)
27 ± 4 μSv/d	1 eV–10 MeV	08/12/2012 to 08/12/2013	Neutron inversion flux from HEND	U.S. NRC, 10 CFR 20.1004	Litvak et al. (2020)
54 ± 3.5 μSv/d.	1 eV–10 MeV	08/12/2012 to 08/12/2013	Neutron inversion flux from HEND	ICRP 74, Table A.42	This study based on Litvak et al. (2020)
83 ± 0.9 μSv/d	~8–100 MeV	11/15/2015 to 01/15/2016	Neutron inversion flux from RAD data (2)	ICRP 74, Table A.42	This study based on Guo, Slaba, et al. (2017), Guo, Zeitlin, et al. (2017)
132 ± 23 μSv/d	1 eV–100 MeV	01/12/2016 to 11/16/2017	Neutron inversion flux from HEND and RAD data	ICRP 74, Table A.42	This study

Note. The dose equivalent rate calculate from Radiation Assessment Detector (RAD) data are limited to the energies between 8 and 1,000 MeV. While the dose equivalent rate calculated from HEND data was limited for energies between 0.01 and 10 MeV.

Equivalent dose, H_T (Sv): The equivalent dose in an organ or tissue T; where $D_{T,R}$ is the mean absorbed dose from radiation of type R in the specified organ or tissue, T. w_R is the radiation weighting factor. This is used for applications when the incident radiation is known (type and energy) where $H_T = \sum_R w_R D_{T,R}$

Effective dose, E (Sv): The tissue weighted sum of equivalent doses in all specified organs and tissues used to estimate the damage to the whole body and often referenced for occupational and lifetime dose limits, w_T is the tissue weighting factor. That is, $E = \sum_T w_T \sum_R w_R D_{T,R} = \sum_T w_T H_T$.

Two earlier studies provide estimates of the neutron dose rates at the surface of Mars based on measurements. The summary of the resulting dose equivalent rates from these studies are presented in the first four rows of Table 3. In one study, Litvak et al. (2020) implemented a methodology to derive neutron flux spectra in orbit covering an energy range from 1 eV to 10 MeV during the period between August 2012 to August 2013. Multiplying the neutron flux spectra with the efficiency curves of HEND detectors provided predicted orbital neutron counts. Then, the simulated neutron spectra in orbit are scaled by a factor of 1.3 to find the corresponding neutron flux spectra at the surface (i.e., like our atmospheric correction described in Section 3.1). The surface neutron flux spectra are then multiplied by the DAN detector efficiency function to determine the expected DAN neutron counts (as done for the orbital neutron flux spectra using the HEND efficiency curves). The best fit for the neutron flux spectra was found using the least squares method by comparing the actual measured counts both from HEND and DAN with the simulated counts. The final reported surface neutron dose equivalent rate was 27 ± 4 μSv/d using the ICRP and International Commission on Radiation units and measurements (ICRU) fluence-to-dose conversion coefficients (Litvak et al., 2020).

The next set of studies of interest consists of three different RAD calculations of the surface neutron doses and fluxes for energies >~10 MeV; (a) Hassler et al. (2014) reported an initial total dose equivalent rate of 640 ± 120 μSv/d using RAD measurements for the first year of MSL (August 2012–August 2014). Later, Köhler et al. (2014) estimated that neutron contribution to the total dose equivalent rate was 61 ± 15 μSv/d (i.e., ~10% of the 640 ± 120 μSv/d); (b) Matthiä et al. (2016) summarized the modeling efforts from different computational transport codes which resulted in the neutron dose equivalent rate ~180 μSv/d (i.e., ~35% of the total dose equivalent rate of the 520 μSv/d); (c) Guo, Zeitlin, et al. (2017) derived the power-law neutron flux spectrum using the DRFs from RAD measurements for the period of November 2015 to January 2016. The corresponding neutron dose equivalent rate was 25.3 ± 3.3 μSv/d, where the neutron flux spectrum, the quality factors, and the conversion coefficients defined by United States Nuclear Regulatory Commission (NRC, 1991) are used to estimate a neutron dose equivalent rate. However, the RAD team later identified a missing normalization factor in the original DRFs that accounts for the cosine-law source distribution in simulations to emulate the isotropic environment (Carlton et al., 2018; McKinney et al., 2006). To correct for this missing factor, the number have to be multiplied by 4. Additionally, the histogram bins format changed after sol 1,220 from 48 bins to 96 bins, and when post-processing the data, instead of re-binning and adding the data for each bin, the data was interpolated which caused the counts to be half of the expected values (i.e., need a correction factor of 2). If we multiply the factors 4 and 2 directly to the neutron dose equivalent rate, the approximation becomes 202.4 ± 26 μSv/d. Because of all the different adjustments done to the RAD neutron data analysis, it has been difficult to determine consistently the neutron dose equivalent rates.

Using our final inverted and complete neutron flux spectra as derived in Section 4.1, we calculated the dose equivalent rate for all locations covering the time between January 2016 and November 2017 as shown in Figure 10a and compiled in the last column of Table 2. To derive the dose equivalent rate from the flux spectrum, we used the conversion coefficients for dose equivalent rate per unit neutron fluences (see Figure 11 from

the ICRP publication 74 Table A.42, ICRP, 1996). This is the first time that the neutron dose equivalent are unequivocally estimated covering the energy range from 0.1 eV up to a few hundred MeV neutrons at the Martian surface based on measurements. This also enabled us to unfold that half of the neutron dose equivalent rate comes from low-energy neutrons (from 1 eV to 10 MeV based on the HEND data) and the other half from high-energy neutrons (>6 MeV based on the RAD data) as presented in Figure 10b. Overall, we estimate an average neutron dose equivalent rate of 132 ± 23 µSv/d for the period 1,200–1,900 sols (last row in Table 3). This value of the dose equivalent rate is the first estimate covering a wide energy range. At the same time, a RAD analysis estimated an average total dose equivalent rate of ∼600 µSv/d for the same period (from charged particles). When we add the dose equivalent rates from charged particles and neutrons, we obtained ∼730 µSv/d. This indicates that our neutron dose equivalent rate corresponds to about 20% of the total dose equivalent at the surface of Mars (This percentage is between the previously cited estimated neutron contribution of 10% and 35%). Based on the neutron dose rate values from measurements (shown in the last column of Table 2) and the simulated neutron dose rates from different transport codes (Matthiä et al., 2016), we can conclude that the neutron dose equivalent rate contribution can range from ∼120 to 180 µSv/d. These values of dose equivalent rate are higher than the previously published estimates (ranging from 25 to 60 µSv/d) (Guo, Zeitlin, et al., 2017; Köhler et al., 2014), likely due to the aforementioned missing factors in earlier RAD studies.

For completeness, we recalculated the dose equivalent rates based on the studies from Litvak et al. (2020) and Guo, Zeitlin, et al. (2017). The estimates of the dose equivalent rates are presented in Table 3 and referenced as "based on" the original studies. We extracted the neutron flux spectra from Figure 5 in Litvak et al. (2020) and fit it with a power-law between 1 eV and 10 MeV to find the respective intensity and spectral index coefficients. Then, using this neutron spectrum, we multiplied it by the dose conversion coefficients used in our study (see Figure 11 and obtained a dose equivalent rate of 54 ± 3.5 µSv/d. Similarly, we corrected (i.e., multiplying it by a factor of 8) the reported RAD flux intensity from Guo, Zeitlin, et al. (2017) and computed the dose equivalent rate
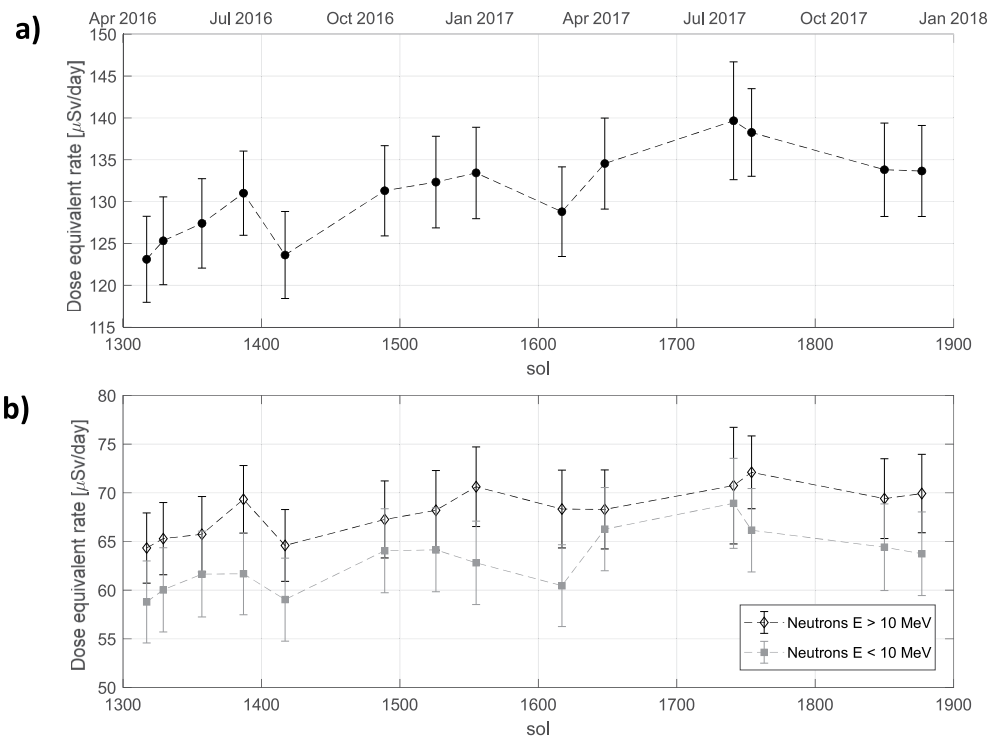

Figure 10. (a) Dose equivalent rate estimates using the International Commission on Radiological Protection conversion coefficients multiplied by the corresponding combined neutron flux spectra as derived from High Energy Neutron Detector and Radiation Assessment Detector data for each location, see Table 2 last column. It is shown that the dose equivalent rates are higher as expected due to the galactic cosmic ray reaching maximum intensity when the solar activity is minimum ∼2019. (b) Dose equivalent rate estimates separated by neutron energy (above and below 10 MeV). The contributions to the total neutron dose equivalent rate are comparable, where neutrons with energies <10 MeV contribute 40%–50% and neutrons with energies >10 MeV contribute 50%–60%.
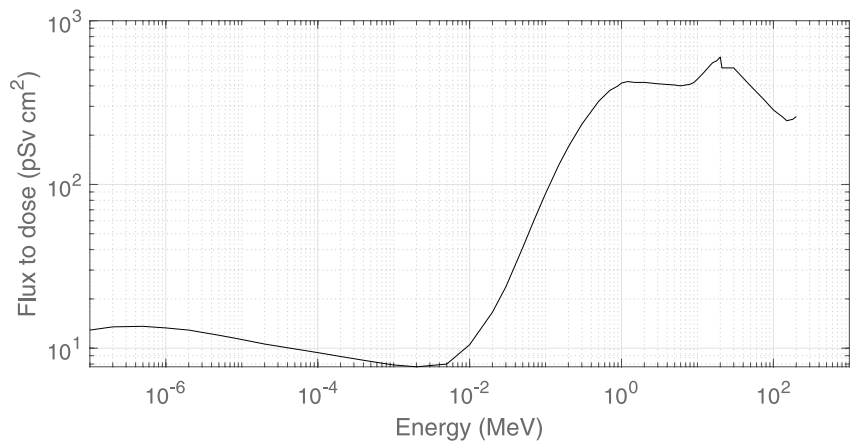
Figure 11. Conversion coefficients for ambient dose equivalent per unit neutron fluences from the International Commission on Radiological Protection (ICRP) publication 74 Table A.42 (ICRP, 1996). Other publications referenced the NRC coefficient (NRC, 1991) or from publication ICRP 60 (ICRP, 1991).

using the coefficients presented in Figure 11b (for energies >10 MeV). The final RAD neutron dose equivalent rate came out to be 83 ± 0.9 μSv/d. Note that both neutron dose equivalent rates recalculated here are different from the published values due to correction factors (for RAD) or the use of a different dose conversion factor (for HEND).

Finally, we investigated how the dose equivalent rates estimated in this study vary with different atmospheric pressure and solar modulation conditions. Figure 12a shows that the neutron dose rate is positively correlated with the atmospheric pressure. Historically, there have been many measurements of GCR-induced neutron fluxes as a function of depth in Earth's atmosphere. These observations indicated that at the top of the Earth's atmosphere (0–~50 g/cm^2, comparable to the Martian atmosphere values), the neutron flux increases as a function of the atmospheric depth until it reaches a maximum (called the Pfotzer maximum). For larger depths (>~50 g/cm^2) into the terrestrial atmosphere, the neutron flux then starts to decrease steadily (Armstrong et al., 1973). In addition, many studies have analyzed the shielding effect of the Martian atmosphere thickness on the surface total dose equivalent rate (including both charged and neutral particles). The results from these studies indicated that as the atmospheric pressure increases, the total dose equivalent from GCRs and
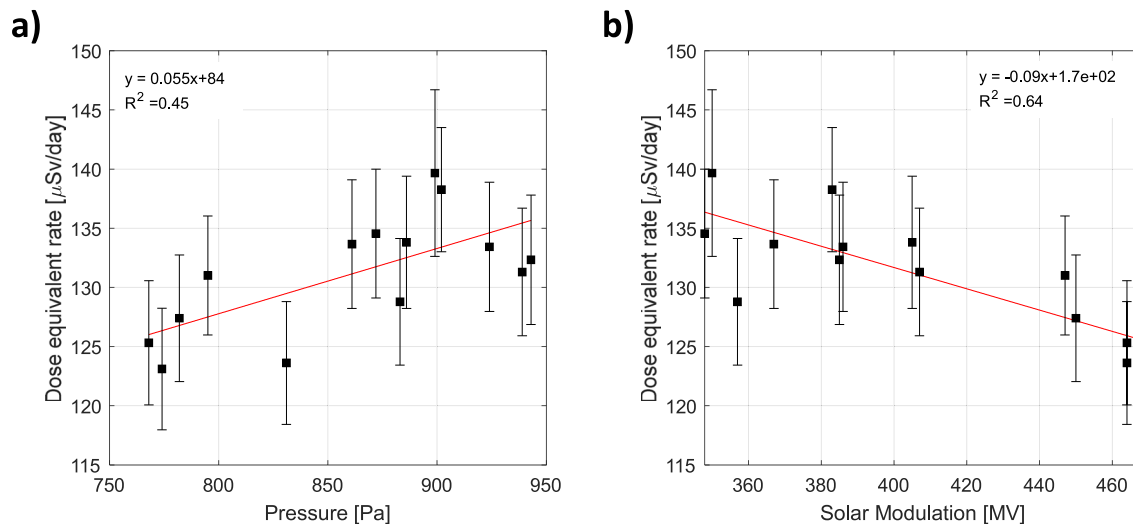

Figure 12. The neutron dose equivalent rate for each location compared with the atmospheric pressure at the surface and solar modulation. (a) Shows the direct correlation between the atmospheric pressure and the dose equivalent rate. As the atmospheric pressure increases the number of neutrons created increases and thus deposit more dose. (b) Shows the inverse correlation between dose and solar modulation. This correlation is expected because at lower solar modulation, the galactic cosmic rays intensity reaches a maximum, creating more neutron when interacting with Mars atmosphere and soil.

secondary particles (from charged and neutral particles) decreases proportionally (Guo, Slaba, et al., 2017; Hassler et al., 2014; Rafkin et al., 2014). However, our study demonstrates that the neutron dose equivalent rates increase proportionally to the atmospheric total column mass/area (pressure) as shown in Figure 12a. As the thickness (pressure) of atmosphere of Mars varies seasonally, it causes a proportional change in the neutron dose.

On the other hand, we correlate the dose equivalent rate to the solar modulation parameter obtained from the Oulu neutron monitor to see if the trend of the solar modulation potential measured at Earth behaves similarly at Mars (Usoskin, 2022). We would expect that the neutron counts at the surface of Mars generated by GCRs will increase as the intensity of the GCRs increases during solar minimum (when the modulation voltage is the lowest). Figure 12b shows how the neutron dose equivalent rate is negatively correlated to the solar modulation (i.e., solar modulation describes the potential that the GCRs experiences as they get attenuated while traversing the solar system (Usoskin et al., 2005)). This happens when the sun's activity increases and the solar magnetic field strengthens, shielding lower energy GCRs and finally causing less neutrons generated within Mars' atmosphere.

5. Discussion and Conclusions

We have developed a new empirical approach that can be used to provide the neutron environment at the Mars surface, using in-situ measurements from MSL-RAD and Odyssey-HEND. The new methodology presented in this paper can help estimate neutron radiation effects for future Martian space exploration missions. Our modeling accounts for the Martian atmosphere's attenuation of neutrons, allowing us to extrapolate the orbital HEND data to the Martian surface. Furthermore, we provide the first estimate of the complete neutron differential flux spectrum at the surface of Mars based on measurements that cover an energy range from 10 eV up to 1 GeV. The neutron spectrum complements the charged particle and other secondary particle spectra, giving a complete picture of the surface radiation environment.

Correspondingly, for the first time we report the neutron dose equivalent rate covering a wider energy range and we can differentiate the dose contributions from different neutron energies, with >10 MeV neutrons contributing about 50% of the total neutron dose. It was found that the previous estimates of doses from high-energy neutrons by RAD were underestimated. We also see how the Martian neutron dose equivalent rates have evolved from models to comparisons with measurements. When using actual measurements, the neutron dose equivalent rate estimates still depend on the instrument, energy range, correction factors, efficiency function, conversion coefficients, methodology, and initial conditions for the power law fit. Previous neutron dose equivalent rate values have not been consistent with each other and are difficult to reconcile.

With our unique approach of using data from different instruments, and correlating that data through modeling, we reevaluated the contribution of neutrons to the total dose. Our result of 20% falls about midway between the measurement-based estimate of roughly 10% of the total dose (Köhler et al., 2014) and the simulation-based estimate of 35% (Matthiä et al., 2016).

Understanding the intricacies of the radiation environment on Mars helps us to estimate and mitigate radiation exposure, reduce risk factors, and monitor the long-term environment. Neutrons are challenging to shield against because they do not lose energy by ionization—they do not possess charge or directly interact with atomic electrons but instead undergo nuclear interactions. In designing future habitats on Mars, ideal shielding materials need to moderate ions, electrons, gamma rays, and fast to thermal neutrons. Because the neutron biological damage depends on the neutron's energy, deriving a neutron flux spectrum over the full neutron energy range (from thermal to fast energies) that is based on actual in-situ measurements is vital to estimate the neutron contribution to the total absorbed dose and effective dose for future crewed exploration missions to Mars.

Data Availability Statement

Data used for this study can be found in the JPL Open Repository (Martinez Sierra, 2023): https://doi.org/10.48577/jpl.S9J00R.

References

Alexander, M. (2001). *Mars transportation environment definition document*. National Aeronautics and Space Administration, Marshall Space Flight Center.

Armstrong, T., Chandler, K., & Barish, J. (1973). Calculations of neutron flux spectra induced in the earth's atmosphere by galactic cosmic rays. *Journal of Geophysical Research*, 78(16), 2715–2726. https://doi.org/10.1029/ja078i016p02715

Balaram, J., Aung, M., & Golombek, M. P. (2021). The ingenuity helicopter on the perseverance rover. *Space Science Reviews*, 217(4), 56. https://doi.org/10.1007/s11214-021-00815-w

Boynton, W. V., Feldman, W. C., Mitrofanov, I. G., Evans, L. G., Reedy, R. C., Squyres, S. W., et al. (2004). The Mars Odyssey gamma-ray spectrometer instrument suite. In C. T. Russell (Ed.), *2001 Mars Odyssey* (pp. 37–83). Springer Netherlands.

Burger, P. A. H. (2000). Cosmic ray modulation strength (Phi) since 1936 for LIS.

Carlton, A., Pich, M. D. S.-S., Kim, W., Jun, I., & Cahoy, K. (2018). Using the galileo solid-state imaging instrument as a sensor of Jovian energetic electrons. *IEEE Transactions on Nuclear Science*, 66(1), 255–261. https://doi.org/10.1109/tns.2018.2883985

Cool, D., & Peterson, H., Jr. (1991). Standards for protection against radiation, 10 CFR part 20: Nuclear regulatory commission.

Cucinotta, F. A., Schimmerling, W., Wilson, J. W., Peterson, L. E., Badhwar, G. D., Saganti, P. B., & Dicello, J. F. (2001). Space radiation cancer risks and uncertainties for Mars missions. *Radiation Research*, 156(5), 682–688. https://doi.org/10.1667/0033-7587(2001)156[0682:srcrau]2.0.co;2

Dibb, S., Hardgrove, C., Gabriel, T., & Czarnecki, S. (2019). Influence of nearby topography on passive neutron count rates from the dynamic albedo of neutrons instrument on the Mars Science Laboratory rover. In *Proceedings 50th annual lunar and planetary science conference* (p. 2908).

Dilillo, L., Bosser, A., Javanainen, A., Virtanen, A., Nakajima, J., Calligaro, C., & Gatti, U. (2018). Space radiation effects in electronics. In C. Calligaro & U. Gatti (Eds.), *Rad-hard semiconductor memories*. River Publishers.

Drake, D. M., Feldman, W. C., & Jakosky, B. M. (1988). Martian neutron leakage spectra. *Journal of Geophysical Research*, 93(B6), 6353–6368. https://doi.org/10.1029/jb093ib06p06353

Drout, M., Piro, A., Shappee, B., Kilpatrick, C., Simon, J., Contreras, C., et al. (2017). Light curves of the neutron star merger GW170817/SSS17a: Implications for r-process nucleosynthesis. *Science*, 358(6370), 1570–1574. https://doi.org/10.1126/science.aaq0049

Ehresmann, B., Hassler, D., Zeitlin, C., Guo, J., Wimmer-Schweingruber, R., Khaksari, S., & Loeffler, S. (2021). Natural radiation shielding on Mars measured with the MSL/RAD instrument. *Journal of Geophysical Research: Planets*, 126(8), e2021JE006851. https://doi.org/10.1029/2021je006851

Farley, K. A., Williford, K. H., Stack, K. M., Bhartia, R., Chen, A., de la Torre, M., et al. (2020). Mars 2020 mission overview. *Space Science Reviews*, 216(8), 1–41. https://doi.org/10.1007/s11214-020-00762-y

Feldman, W., Boynton, W. V., Tokar, R., Prettyman, T., Gasnault, O., Squyres, S., et al. (2002). Global distribution of neutrons from Mars: Results from Mars Odyssey. *Science*, 297(5578), 75–78. https://doi.org/10.1126/science.1073541

Forbush, S. E. (1938). On world-wide changes in cosmic-ray intensity. *Physical Review*, 54(12), 975–988. https://doi.org/10.1103/physrev.54.975

Gómez-Elvira, J., Armiens, C., Castañer, L., Domínguez, M., Genzer, M., Gómez, F., et al. (2012). REMS: The environmental sensor suite for the Mars Science Laboratory rover. *Space Science Reviews*, 170(1–4), 583–640. https://doi.org/10.1007/s11214-012-9921-1

Grotzinger, J. P., Crisp, J., Vasavada, A. R., Anderson, R. C., Baker, C. J., Barry, R., et al. (2012). Mars Science Laboratory mission and science investigation. *Space Science Reviews*, 170(1–4), 5–56. https://doi.org/10.1007/s11214-012-9892-2

Guo, J., Khaksarighiri, S., Wimmer-Schweingruber, R. F., Hassler, D. M., Ehresmann, B., Zeitlin, C., et al. (2021). Directionality of the Martian surface radiation and derivation of the upward albedo radiation. *Geophysical Research Letters*, 48(15), e2021GL093912. https://doi.org/10.1029/2021gl093912

Guo, J., Lillis, R., Wimmer-Schweingruber, R. F., Zeitlin, C., Simonson, P., Rahmati, A., et al. (2018). Measurements of Forbush decreases at Mars: Both by MSL on ground and by MAVEN in orbit. *Astronomy & Astrophysics*, 611, A79. https://doi.org/10.1051/0004-6361/201732087

Guo, J., Slaba, T. C., Zeitlin, C., Wimmer-Schweingruber, R. F., Badavi, F. F., Böhm, E., et al. (2017). Dependence of the Martian radiation environment on atmospheric depth: Modeling and measurement. *Journal of Geophysical Research: Planets*, 122(2), 329–341. https://doi.org/10.1002/2016je005206

Guo, J., Zeitlin, C., Wimmer-Schweingruber, R., Hassler, D. M., Köhler, J., Ehresmann, B., et al. (2017). Measurements of the neutral particle spectra on Mars by MSL/RAD from 2015-11-15 to 2016-01-15. *Life Sciences and Space Research*, 14, 12–17. https://doi.org/10.1016/j.lssr.2017.06.001

Hassler, D. M., Zeitlin, C., Wimmer-Schweingruber, R., Böttcher, S., Martin, C., Andrews, J., et al. (2012). The radiation assessment detector (RAD) investigation. *Space Science Reviews*, 170(1–4), 503–558. https://doi.org/10.1007/s11214-012-9913-1

Hassler, D. M., Zeitlin, C., Wimmer-Schweingruber, R. F., Ehresmann, B., Rafkin, S., Eigenbrode, J. L., et al. (2014). Mars' surface radiation environment measured with the Mars Science Laboratory's Curiosity rover. *Science*, 343(6169), 1244797. https://doi.org/10.1126/science.1244797

Hess, W. N., Patterson, H. W., Wallace, R., & Chupp, E. L. (1959). Cosmic-ray neutron energy spectrum. *Physical Review*, 116(2), 445–457. https://doi.org/10.1103/physrev.116.445

Huff, J., & Cucinotta, F. A. (2009). *Risk of degenerative tissue or other health effects from radiation exposure: Human Health and performance risks of space exploration missions* (pp. 213–235). National Aeronautics and Space Administration, NASA SP-2009-3405.

ICRP. (1991). Publication 60: 1990 recommendations of the international commission on radiological protection. In *Annals of the ICRP* (Vol. 21).

ICRP. (1996). Publication 74: Conversion coefficients for use in radiological protection against external radiation (Vol. 23).

ICRP. (2010). Publication 116: Conversion coefficients for radiological protection quantities for external radiation exposures. *Annals of the ICRP*, 40(2–5), 1–258.

Jun, I., Garrett, H. B., & Evans, R. W. (2019). Trapped particle environments at the outer planets. *IEEE Transactions on Plasma Science*, 47(8), 3923–3930. https://doi.org/10.1109/tps.2019.2907069

Jun, I., Mitrofanov, I., Litvak, M. L., Sanin, A. B., Kim, W., Behar, A., et al. (2013). Neutron background environment measured by the Mars Science Laboratory's Dynamic Albedo of Neutrons instrument during the first 100 sols. *Journal of Geophysical Research: Planets*, 118(11), 2400–2412. https://doi.org/10.1002/2013je004510

Justh, H., & Justus, C. (2007). Mars global reference atmospheric model (Mars-GRAM 2005) applications for Mars Science Laboratory mission site selection processes. In *Proceedings 7th international conference on Mars 2007*.

Köhler, J., Zeitlin, C., Ehresmann, B., Wimmer-Schweingruber, R., Hassler, D., Reitz, G., et al. (2014). Measurements of the neutron spectrum on the Martian surface with MSL/RAD. *Journal of Geophysical Research: Planets*, 119(3), 594–603. https://doi.org/10.1002/2013je004539

Lario, D. (2005). Advances in modeling gradual solar energetic particle events. *Advances in Space Research*, 36(12), 2279–2288. https://doi.org/10.1016/j.asr.2005.07.081

Litvak, M., Sanin, A., Mitrofanov, I., Bakhtin, B., Jun, I., Martinez-Sierra, L., et al. (2020). Mars neutron radiation environment from HEND/Odyssey and DAN/MSL observations. *Planetary and Space Science*, *184*, 104866. https://doi.org/10.1016/j.pss.2020.104866

Martinez Sierra, L. M. (2023). Data set for the article: Unfolding the neutron flux spectrum on the surface of Mars using the MSL-RAD and Odyssey-HEND data. JPL Open Repository, v1. https://doi.org/10.48577/jpl.S9J00R

Matthiä, D., Ehresmann, B., Lohf, H., Köhler, J., Zeitlin, C., Appel, J., et al. (2016). The Martian surface radiation environment–a comparison of models and MSL/RAD measurements. *Journal of Space Weather and Space Climate*, *6*, A13. https://doi.org/10.1051/swsc/2016008

Matthiä, D., Hassler, D. M., de Wet, W., Ehresmann, B., Firan, A., Flores-McLaughlin, J., et al. (2017). The radiation environment on the surface of Mars-Summary of model calculations and comparison to RAD data. *Life Sciences and Space Research*, *14*, 18–28. https://doi.org/10.1016/j.lssr.2017.06.003

McKinney, G., Lawrence, D., Prettyman, T., Elphic, R., Feldman, W., & Hagerty, J. (2006). MCNPX benchmark for cosmic ray interactions with the Moon. *Journal of Geophysical Research*, *111*(E6), E06004. https://doi.org/10.1029/2005je002551

McSween, H. Y., Jr., & Huss, G. R. (2010). *Cosmochemistry*. Cambridge University Press.

Mewaldt, R. (1994). Galactic cosmic ray composition and energy spectra. *Advances in Space Research*, *14*(10), 737–747. https://doi.org/10.1016/0273-1177(94)90536-3

Mitrofanov, I., Anfimov, D., Kozyrev, A., Litvak, M., Sanin, A., Tret'yakov, V., et al. (2002). Maps of subsurface hydrogen from the high energy neutron detector, Mars Odyssey. *Science*, *297*(5578), 78–81. https://doi.org/10.1126/science.1073616

Mitrofanov, I., Litvak, M., Varenikov, A., Barmakov, Y., Behar, A., Bobrovnitsky, Y., et al. (2012). Dynamic Albedo of Neutrons (DAN) experiment onboard NASA's Mars Science Laboratory. *Space Science Reviews*, *170*(1–4), 559–582. https://doi.org/10.1007/s11214-012-9924-y

Nelson, G. A. (2016). Space radiation and human exposures, a primer. *Radiation Research*, *185*(4), 349–358. https://doi.org/10.1667/rr14311.1

NOAA. (2017). Solar flare event from GOES-15 data.

NRC. (1991). Part 20—Standards for protection against radiation.

O'Gallagher, J., & Simpson, J. (1965). Search for trapped electrons and a magnetic moment at Mars by Mariner IV. *Science*, *149*(3689), 1233–1239. https://doi.org/10.1126/science.149.3689.1233

Pelowitz, D. (2013). MCNP6 user's manual (Los Alamos National laboratory): LA-CP-00634, May.

Rafkin, S. C., Zeitlin, C., Ehresmann, B., Hassler, D., Guo, J., Köhler, J., et al. (2014). Diurnal variations of energetic particle radiation at the surface of Mars as observed by the Mars Science Laboratory Radiation Assessment Detector. *Journal of Geophysical Research: Planets*, *119*(6), 1345–1358. https://doi.org/10.1002/2013je004525

Reedy, R. C., & Arnold, J. (1972). Interaction of solar and galactic cosmic-ray particles with the Moon. *Journal of Geophysical Research*, *77*(4), 537–555. https://doi.org/10.1029/ja077i004p00537

Stricklin, D. L., VanHorne-Sealy, J., Rios, C. I., Scott Carnell, L. A., & Taliaferro, L. P. (2021). *Neutron radiobiology and dosimetry*. Radiation Research Society.

Usoskin, I. G. (2022). *Cosmic ray station of the University of Oulu, Sodankyla Geophysical Observatory* (Vol. 2022). University of Oulu.

Usoskin, I. G., Alanko-Huotari, K., Kovaltsov, G. A., & Mursula, K. (2005). Heliospheric modulation of cosmic rays: Monthly reconstruction for 1951–2004. *Journal of Geophysical Research*, *110*(A12), A12108. https://doi.org/10.1029/2005ja011250

Weisstein, E. W. (2002). Least squares fitting. Retrieved from https://mathworld.wolfram.com/

Wiedenbeck, M., Binns, W., Cummings, A., Davis, A., de Nolfo, G., Israel, M., et al. (2007). An overview of the origin of galactic cosmic rays as inferred from observations of heavy ion composition and spectra. *Space Science Reviews*, *130*(1), 415–429. https://doi.org/10.1007/s11214-007-9198-y

Zeitlin, C., Hassler, D., Wimmer-Schweingruber, R., Ehresmann, B., Appel, J., Berger, T., et al. (2016). Calibration and characterization of the radiation assessment detector (RAD) on curiosity. *Space Science Reviews*, *201*(1), 201–233. https://doi.org/10.1007/s11214-016-0303-y